Article
Vol. 22, No. 2, p. 227–239, April 2018
http://dx.doi.org/10.1007/s12303-017-0028-2
pISSN 1226-4806 eISSN 1598-7477
Geosciences Journal GJ

Across-fault distributions of radon concentrations in soil gas for different tectonic environments

Xiaolong Sun[1]*, Pengtao Yang[1], Yang Xiang[2], Xueyun Si[3], and Dongying Liu[1]

[1]Key Laboratory of Crustal Dynamics, Institute of Crustal Dynamics, China Earthquake Administration, Beijing 100085, China
[2]Earthquake Administration of Xinjiang Uygur Autonomous Region, Urumqi 830002, China
[3]Earthquake Administration of Ningxia Hui Autonomous Region, Yinchuan 750001, China

ABSTRACT: The radon concentration in soil gas at the crustal surface is closely related to the development of local fractures. Therefore, the spatial variation in soil-gas radon concentrations across faults differs between fault zones located in different tectonic environments. This study investigates the Beiluntai thrust fault and the Haiyuan strike-slip fault in west China, which are assumed to be typical examples of the different types of faults. Radon concentrations in soil gas were measured at various locations around these faults, and the spatial variation in these concentrations was characterized along fault-perpendicular profiles. For normal fault, our results indicate that concentrations are usually highest at the fault, and decrease gradually away from the fault in either direction. For thrust, however, concentrations increase in the hanging wall approaching the fault, but decrease sharply at the fault. For strike-slip fault with extension across the fault, soil-gas radon concentrations are relatively high at the fault, and decrease gradually with distance from the fault. For strike-slip fault with contraction across the fault, soil-gas radon concentrations are relatively low at the fault, and increase gradually with distance from the fault.

Key words: fault-crossing profile, soil-gas radon, fault zone, spatial distribution

Manuscript received November 9, 2016; Manuscript accepted May 8, 2017

1. INTRODUCTION

Radon (Rn) gas is produced by the decay of the uranium radioisotope ^{238}U, and is the progeny of radioactive radium ^{226}Ra. Radon is created in solid or liquid phases containing radium. It is well known that radioactive nuclides of the ^{238}U decay chain occur with varying concentrations in Earth's crust and can be found in almost all types of soil, rocks, granite, and sand (Kobeissi et al., 2008, 2013, 2015; Cho et al., 2015). Specifically, radon emits alpha particles with an decay energy of 5.8 MeV, and can move through crustal reservoirs with a half-life of 3.82 days, after which it enters the atmosphere and local environment (Nazaroff, 1992). When ^{226}Ra decays, ^{222}Rn atoms can be ejected from soil grains by alpha recoil, thus transferring into groundwater or air, and finally escaping into the atmosphere (Abdallah et al., 2007; Somlai et al., 2007; Tabar and Yakut, 2014).

*Corresponding author:
Xiaolong Sun
Key Laboratory of Crustal Dynamics, Institute of Crustal Dynamics, China Earthquake Administration, Beijing 100085, China
Tel: +86-13810527099, Fax: +86-10-62842632, E-mail: xlsun04@163.com

Radon is a naturally occurring radioactive gas produced in the Earth's crust due to alpha-decay of radium. It migrates freely through soil, either by molecular diffusion or advection, and is then released to the atmosphere, where its behavior and distribution are governed mainly by meteorological processes (Catalano et al., 2015). Depending on the material porosity and velocity of interstitial fluid, radon can be transported great distances by advection. The unique properties of soil-gas radon make it useful as a tracer of geological processes, including uranium exploration (Wattananikorn et al., 1995; Mudd, 2008), monitoring of volcanic (Immè et al., 2006) and seismic activity (Baykara et al., 2009; Namvaran and Negarestani, 2013), and atmospheric studies (Zahorowski et al., 2014).

Many investigators have used radon measurements to monitor seismic activity because radon is both radioactive and a chemically inert noble gas. The relatively short half-life (3.82 days) of radon means that radon concentration changes are indicative of recent changes in the subsurface and hence are an important precursor of tectonic activity. Radon anomalies in soil gas and groundwater are commonly observed prior to earthquake ruptures and volcanic eruptions; consequently, they have attracted considerable attention in studies of precursory geochemical signals (King

et al., 1995; Linde and Sacks, 1998; Roeloffs, 1999; Trique et al., 1999; Tuccimei et al., 2015). Increases in radon emission rates are correlated with stress and/or strain energy accumulation along fault system boundaries, and are a short-term indicator of a potential earthquake occurrence (Kobeissi et al., 2015). Changes in soil-gas radon emissions along fault traces can be interpreted as precursory signals of seismic activity and used for earthquake prediction. This hypothesis is supported by the observed correlation between increases in radon exhalation rates and earthquake occurrences.

Various researchers have attempted to correlate radon concentrations with factors such as geology, soil porosity, shears and faults (Przylibski, 2000; Choubey et al., 2001; Wiegand, 2001; Idriss et al., 2014). Mathematical morphology is applied along with the Radon transform to extract the features needed for fault classification (Sulochana al., 2015). Radon spectral-line widths reflect the presence of a fault damage zone across the fault trace, which implies the presence of fractures in the zone around the fault plane. These fractures result from stresses and shearing processes that occur along the fault boundaries (Kobeissi et al., 2015).

Radon gas is used by the scientific community as a tracer of natural phenomena linked to soil degassing along faults, fractures, and crustal discontinuities (King et al., 1996; Choubey et al., 1999; Jönsson et al., 1999; Mazur et al., 1999). Recently, radon has also been used to investigate the dynamics of active faults (Immè et al., 2006; Neri et al., 2006, 2007, 2011; La Delfa et al., 2007; Giammanco et al., 2009; Siniscalchi et al., 2010). The release of soil-gas radon is controlled by factors such as geological structure, lithology, uranium mineralization, and soil thickness; however, proximity to the fault plane and bedrock lithology are the dominant controls on soil-gas radon emissions (Choubey et al., 1999). Soil-gas radon measurements at the Peceneaga–Camena Fault (Dobrogea, Romania) produced a consistent and clear signal that enabled the existence and position of the fault zone to be inferred from the location of the peak radon concentrations (Cosma et al., 2014). In addition, the highest radon concentrations were recorded in intensely fractured areas, consistent with the presence of shallow fractures (Zarroca et al., 2012).

This study investigates the spatial variation in concentrations of soil-gas radon across faults to assess the influence of fault motion and states of strain across faults on radon concentrations. To this end, we measured the concentration of soil-gas radon across two typical faults: the Beiluntai (BLT) thrust fault and the Haiyuan (HY) strike-slip fault.

2. STUDY AREAS

The radon concentration in soil gas at the ground surface is closely related to the extent of local fracturing and the state of strain at the measurement location (Choubey et al., 1999; Roeloffs, 1999). We took measurements of soil-gas radon concentrations for two typical faults: the BLT fault at the northern margin of the Tarim Plate in China, and the HY fault at the northeastern margin of the Qinghai–Tibet Plateau (Fig. 1). We analyzed the results to assess the factors controlling soil-gas radon concentrations along profiles across different types of fault zones.

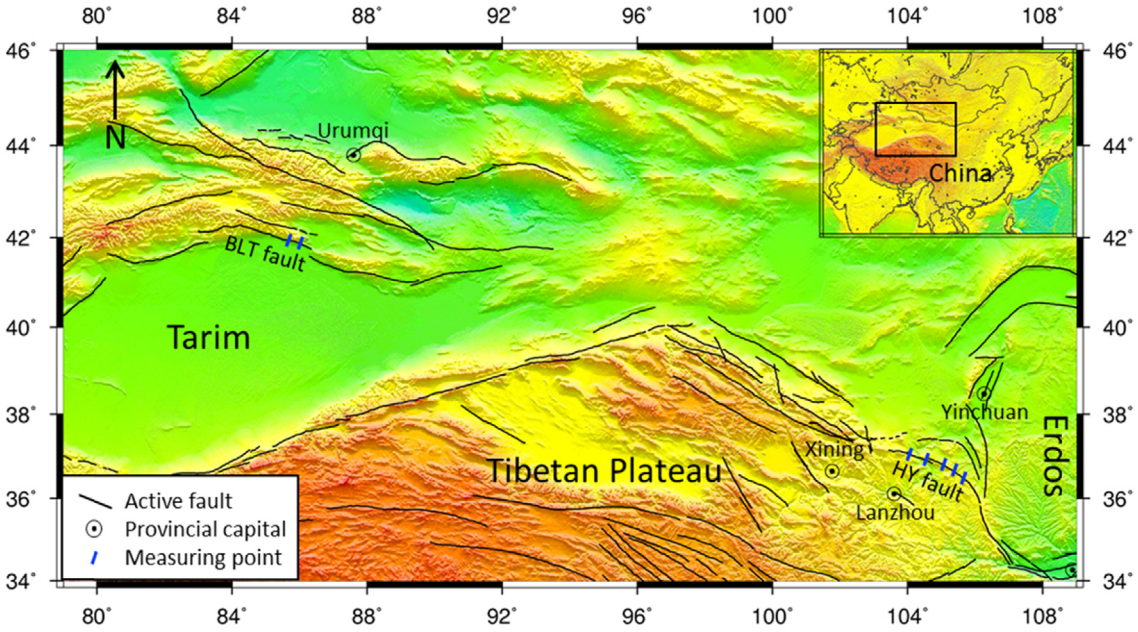

Fig. 1. Map of the study area, showing the locations of measurements of radon concentrations in soil gas across the Beiluntai (BLT) and Haiyuan (HY) faults.

The BLT fault is located on the northern margin of Ak Tag mountain, near Huola mountain, and forms the boundary of the secondary tectonic unit known as the Tarim Plate (Fig. 1). This fault also demarcates the boundary between a Proterozoic metamorphic rock series and a Paleozoic–Cenozoic series. The BLT fault is a thrust that has undergone two tectonic events since the late Pleistocene, with the second event having occurred at the end of this period (Luo and Xiang, 2002).

The HY fault forms part of a major left-lateral fault system at the northeastern margin of the Qinghai–Tibet Plateau. Two great earthquakes (M = 8) are known to have occurred along this fault in 1920 and 1927 (Cavalié et al., 2008). The fault forms the southwestern boundary of the arcuate tectonic region created from the overlap of the Qinghai–Tibet Plateau and the Erdos block (Fig. 1). The fault consists of more than 10 sub-faults, arranged in a stair-step pattern with a total length of ~200 km; several pull-apart basins occur between these sub-faults. Prior to the Quaternary, the HY fault was a contractional fault; however, subsequent changes in the regional stress field mean that the present-day faulting style is left-lateral strike-slip (Liu-Zeng et al., 2007).

3. SAMPLING AND METHODS

The radon concentration in soil gas C_{Rn} (Bq/m^3) was measured using an AlphaGuard PQ 2000 PRO (AG) radon monitor, a soil-gas probe, and an Alpha-Pump (AP; Genitron, Germany) (Fig. 2a). Soil gas was pumped through the AG ionization chamber at a flow rate of 0.5 L/min. The temporary radon (i.e., ^{222}Rn) concentrations were registered at 1-minute intervals over a period of ~20 minutes. After initial growth, the measured concentration stabilizes after ~5 minutes (Fig. 2b). The soil-gas radon concentration is then taken as the average of the final few values measured after stabilization. At the low flow rate we used in this study, the contribution of thoron (^{220}Rn, half-life 55 s) to our soil-gas radon concentration measurements is negligible (Žunić et al., 2006).

Changes in meteorological conditions, such as soil moisture, air temperature, and atmospheric pressure, can affect measurements of soil-gas radon. To mitigate against these influences, we completed all 15 measurements for each measuring line in a single day. Before sampling, holes with a diameter of 3 cm and depth of 80 cm were drilled in the soil using drilling rods. Immediately after removal of the drilling rods, conical gas samplers were inserted to collect the soil gas. Foreign gas in the samplers and the rubber tube connecting the samplers to the vacuum pump was extracted and removed prior to commencing signal counting. While measuring, we recorded the air temperature and pressure to calibrate the measured radon concentrations in soil gas. The calibration was applied using the relations

$$\left.\begin{aligned} C_{Rn}^{P} &= C_{Rn}^{0}\cdot\left(1-a\cdot\frac{P-1013}{1013}\cdot\frac{P}{P-620}\right),\\ C_{Rn}^{P} &= C_{Rn}^{0}\cdot\left(1+b\cdot\frac{T-20}{293}\cdot\frac{130}{130-T}\right), \end{aligned}\right\} \quad (1)$$

where P is atmospheric pressure, T is temperature, C^{0}_{Rn} is the radon concentration reading obtained directly from the instrument, and C^{P}_{Rn} is the pressure-calibrated radon concentration. C^{T}_{Rn} is the radon concentration after temperature calibration to C^{P}_{Rn}, and represents the final corrected radon concentration. When C^{0}_{Rn} < 30,000 Bq/m^3, the coefficients a and b were set to values of 0.18 and 0.97, respectively; otherwise, values of 0.31 and 0.46 were used.

As shown in Figure 2b, the radon concentration readings tended to stabilize after the third measurement, with only relatively small variations being seen subsequent to this time. At each measurement time, between 20 and 25 readings were

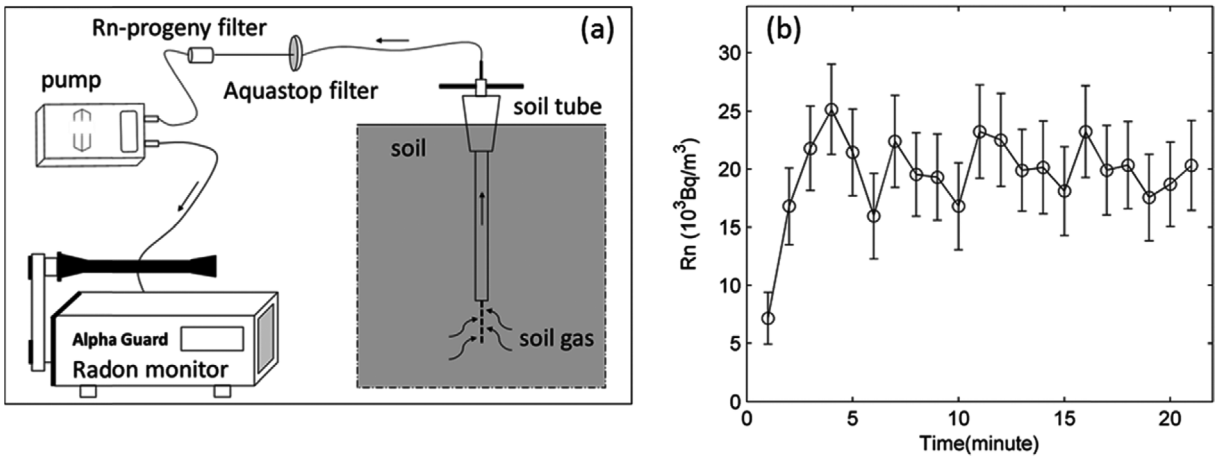

Fig. 2. Soil-gas radon measurement apparatus (a), and example of a measured radon concentration curve (b).

http://dx.doi.org/10.1007/s12303-017-0028-2

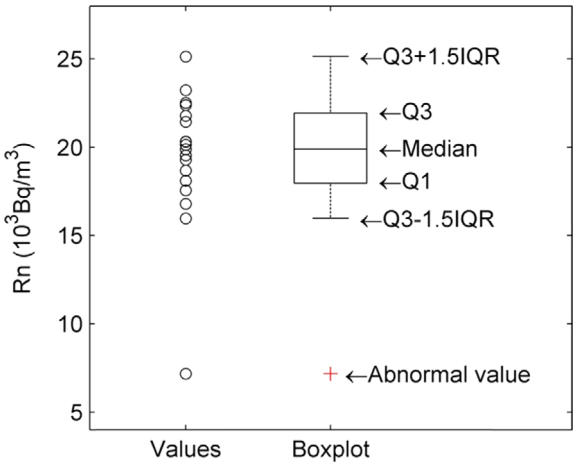

Fig. 3. Illustration of the boxplot method used to analyze soil-gas radon concentrations.

acquired and analyzed using the boxplot method, yielding a characteristic concentration value (Fig. 3). Boxplot analysis, also known as box-whisker plot analysis, uses the minimum, first quartile, median, third quartile, and maximum values of a dataset to describe the data distribution. This method can be applied to evaluate the approximate degree of symmetry and scatter in the dataset, and is particularly useful for comparing data distributions acquired at different sampling times. In a boxplot, the upper and lower edges of the box represent the first (Q1) and third quartile (Q3) of the dataset. The horizontal line inside the box denotes the median value. There two line segments outside the box represent Q3 + 1.5 × IQR and Q1 – 1.5 × IQR, where IQR is the interquartile range (i.e., Q3–Q1). These two lines correspond to so-called inner limits of the dataset; i.e., the values at which outliers are truncated. Data points inside the inner limits are considered to represent normal values for this dataset, whereas those lying outside the inner limits are considered outliers and denoted by "+" symbols in Figures 3–7.

4. RESULTS

We took measurements at five sites along the HY strike-slip fault zone, from west to east, at Santang, Shuiquan, Wanjia, Caiyuan, and Caowa (Fig. 1). Two profiles were measured across the eastern part of the BLT thrust, at Tiemenguan and Korla. We measured soil-gas radon concentration profiles across the faults at these sites, and performed a statistical analysis of the data using the methods described above.

4.1. Strike-Slip Fault

Figure 4 shows the location of sampling points for the profile at Santang (Fig. 4a), which crosses the HY fault zone, and the corresponding soil-gas radon data (Fig. 4b). The HY fault is a typical strike-slip fault with a minor thrust component, and trends WNW at this location, as indicated by the red line in Figure 4a. The southern side of the fault moves westwards relative to the northern side, and, in comparison to the fairly flat topography of the northern block, displays a relatively large amount of relief.

The location of the measurement line at Santang was chosen to be approximately perpendicular to the fault, and extends in both directions away from the fault, with a total length of ~2 km. Measurements were taken at a total of 16 sites along this line, numbered 1 to 16 from south to north in Figure 4a. Figure 4b shows the distribution of soil-gas radon concentrations measured at the 16 sites, with the position of the fault is indicated by the thick gray line. Generally speaking, samples taken away from the fault appear to have higher radon concentrations than those collected at or near the fault. Radon concentrations decrease gradually approaching the fault (e.g., from sampling points 4 to 7, and from 11 to 7), with the minimum concentration obtained at the fault. It has been proposed that radon concentrations in soil gas are strongly influenced by the extent of fracture

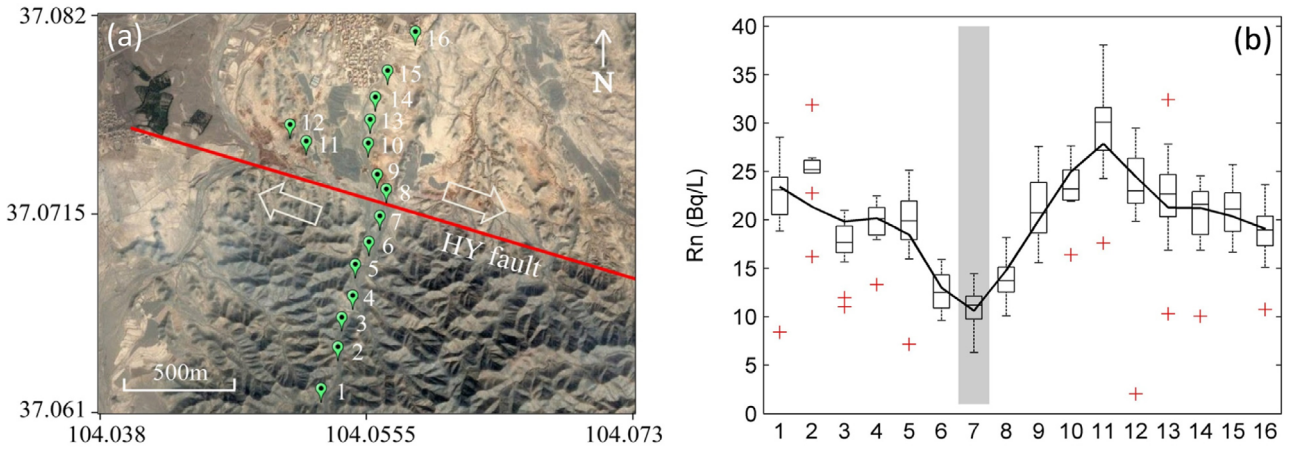

Fig. 4. Sampling locations along the soil-gas radon concentration profile across the Haiyun fault zone at Santang (a) and corresponding data (b).

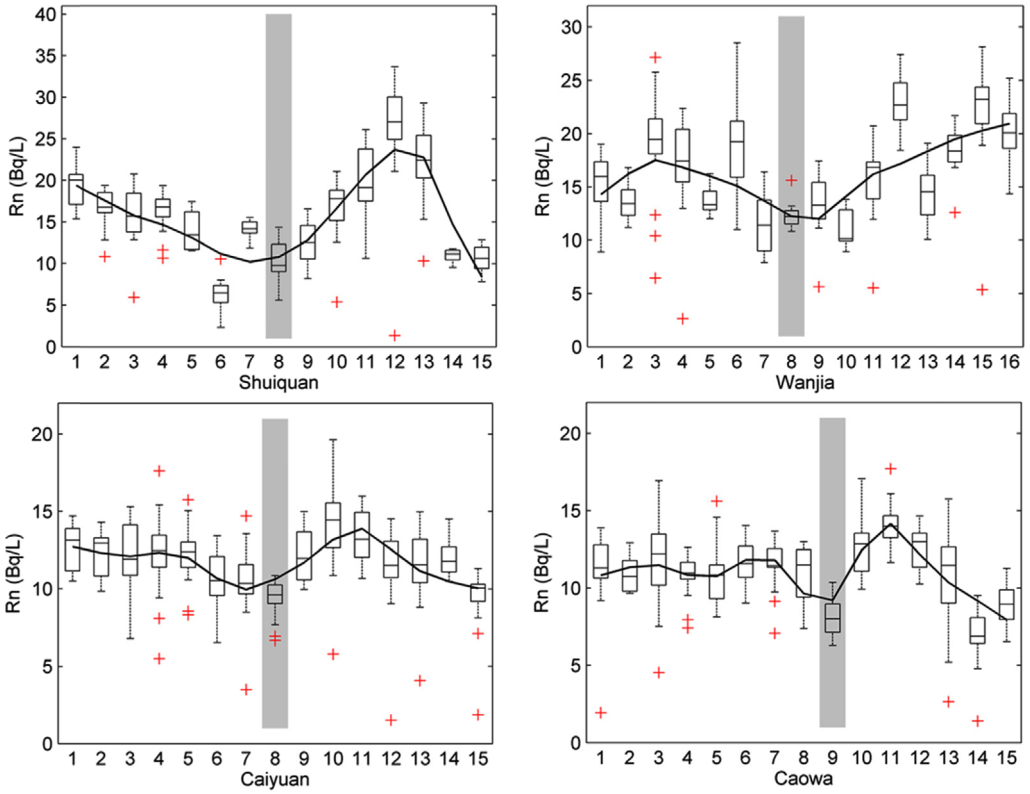

Fig. 5. Soil-gas radon concentrations recorded along four profiles across the HY fault zone.

development in fault zones, shattered zones, and wall rocks (Roeloffs, 1999). The pattern of soil-gas radon concentrations measured across the HY fault at Santang suggests a decreasing level of fracture development with increasing proximity to the fault, reflecting the effect of contractional strain.

The four other profiles measured across the HY fault zone, at Shuiquan, Wanjia, Caiyuan, and Caowa, show soil-gas radon patterns that are similar to those observed at Santang (Fig. 5). Overall, the low radon concentrations at the fault are more evident in the western part of the HY fault zone at Santang and Shuiquan than in the east at Caiyuan and Caowa.

4.2. Thrust Fault

Figure 6 shows the location of sampling points along the profile at Tiemenguan (Fig. 6a), which crosses the BLT fault zone, and the corresponding soil-gas radon data (Fig. 6b). The BLT fault is a typical thrust with a minor strike-slip component, and trends approximately east-west at this location (red line in Fig. 6a). The hanging wall lies on the northern side of the fault, and is characterized by uplifted terrain and high relief. The topography becomes increasingly flat with distance southwards across the footwall block away from the fault.

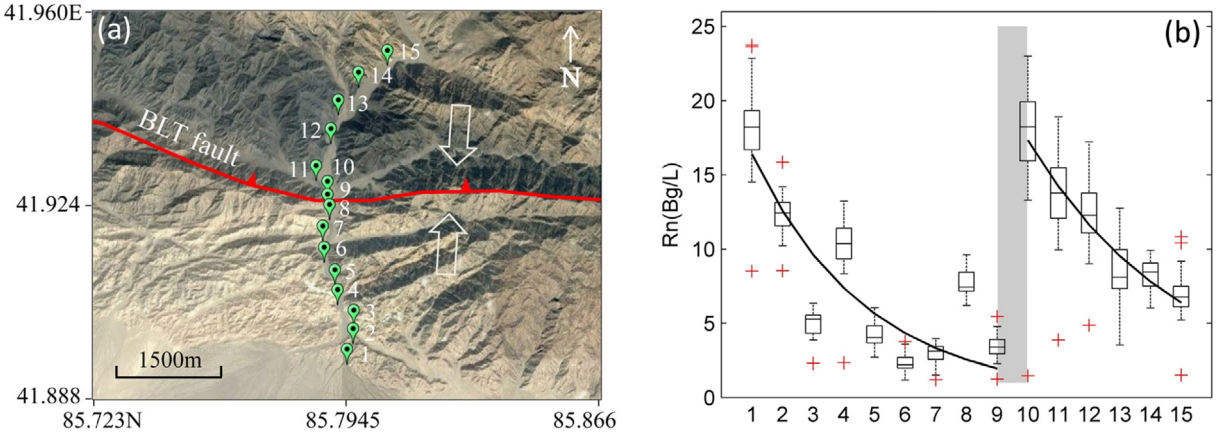

Fig. 6. Sampling locations along the soil-gas radon concentration profile across the BLT fault zone at Tiemenguan (a) and corresponding data (b).

http://dx.doi.org/10.1007/s12303-017-0028-2

The location of the measurement line at Tiemenguan was chosen to be approximately perpendicular to the fault, and it extends in both directions away from the fault, with a total length of ~2.5 km. Measurements were taken at a total of 15 sites along this line, numbered 1 to 15 from south to north in Figure 6a. Figure 6b presents the distribution of soil-gas radon concentrations measured at the 15 sites, with the position of the fault indicated by the thick gray line. In the footwall block, radon concentrations decrease northwards towards the fault (i.e., from sites 1 to 9), reaching a minimum value at the fault. In contrast, radon concentrations decrease away from the fault in the hanging wall (i.e., from sites 10 to 15), with the maximum value just north of the fault. The pattern of soil-gas radon concentrations measured across the BLT fault at Tiemenguan suggests that fractures are much better developed in the hanging wall near to the fault than in the footwall, reflecting the effect of extensional strain. These fractures likely result from the thrusting processes of the fault. The hanging wall has experienced buckling at the near-fault sampling site due to uplift of the surface, leading to localized extensional effects and thus more fractures that promote the escape of soil-gas radon.

4.3. Normal Fault

The BLT fault lies at the junction of the South Tianshan fold zone and the Tarim platform. The fault's eastern segment bifurcates to the north of the city of Korla. One fault branch extends eastwards, continuing along the original trend, after which it merges with the Xinge fault; the other branch deflects toward the southeast. The junction of the eastern segment of the BLT fault and the western end of the Xinge Fault is situated near Korla, and secondary faults are well developed in this area (Fig. 7a). In the excavations surrounding the seismic station at Korla (labelled Obs_hole on Fig. 7a), Proterozoic slate is seen to thrust southwards on top of late Pleistocene glutenite and overlying slope-deposited breccia. The section is covered by a layer of recent slope breccia that is tens of centimeters thick (Fig. 7c).

Based on the above, although the BLT fault is a thrust, it has developed extensional fractures locally, particularly in the uplifted part of the hanging wall. Conversely, the secondary faults (F1–F3 in Fig. 7b) are fairly well developed around the junction of the eastern BLT fault and the western Xinge fault. Depending on the orientations of the secondary faults relative to the principal compressional stress, extensional fracturing may be possible to occur locally. The extensional fractures would remain open in the fault zone, potentially facilitating the escape of soil-gas radon from below to the ground surface or atmosphere. As a result, higher radon concentrations would be measured in the soil gas. Figure 7b shows the distribution of soil-gas radon concentrations measured across the junction of the BLT and Xinge faults. Measurement sites 6, 10, and 12 are adjacent to secondary faults and show elevated soil-gas radon concentrations. The radon concentration at site 10 exceeds 100 Bq/L, much higher than that measured at any other site. This anomaly likely arose because this site is located at the junction between two faults with different orientations. Consequently, shallow crustal rocks at such a junction are relatively prone to being deformed or fractured, providing abundant channels through which soil-gas radon can escape.

5. DISCUSSION

Tuccimei et al. (2010) demonstrated that negative radon anomalies in soil gas and groundwater can be explained by the deformation of loosely consolidated and/or highly porous rocks due to a pore-collapse process that reduces the radon exhaling surface area. In contrast, Mollo et al. (2011) found no significant changes in radon concentrations prior to an earthquake rupture, due to a lack of deformation of strong low-porosity crystalline

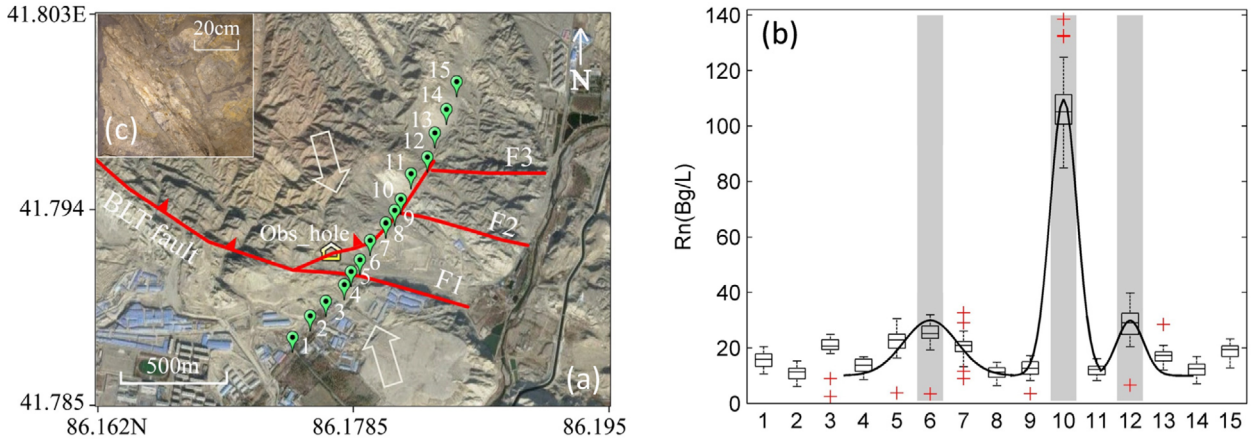

Fig. 7. Sampling locations along the soil-gas radon concentration profile across the BLT fault zone at Korla (a) and corresponding data (b).

igneous rocks. Only after failure, when a macroscopic rupture surface develops in the form of an earthquake rupture plane, was a significant increase in radon emissions recorded.

Tuccimei et al. (2015) found that both negative and positive radon anomalies could be recorded prior to ruptures in the same rock type, depending on the prevailing deformation mechanism. This observation means that pore collapse due to low-stress conditions may cause a significant decrease in radon emissions until a steady-state concentration is achieved (Tuccimei et al., 2010). If low-stress conditions persist over time (e.g., for days or perhaps even weeks and months), the radon signal will not change after rock compaction. Conversely, micro-fracturing due to high-stress conditions leads to the formation of new emission surfaces and a substantially increased radon signal, even though the applied stress remains constant over time. Rock failure, (e.g., an earthquake) creates much larger emission surfaces in the form of macroscopic faults and results in most radon release being concentrated in the faulted area (Mollo et al., 2011).

5.1. Effect of Extent of Fracture Development on Soil-gas Radon Concentration

The recoil energy of radon gas enables it to migrate in porous and permeable media, thus allowing it to escape from the subsurface into the atmosphere. The migration of radon from a geological formation into its surroundings depends on the structure, permeability, and porosity of the geological medium. Migration also depends on grain packing, the type of crystal lattice, and the presence of granite (Kobeissi et al., 2013). The surface and subsurface conditions, soil moisture content in different rock types, and the soil-air pressure difference also affect migration rates. Some wells showing high radon levels occur near fault systems; therefore, radon appears to seep upwards from depth, possibly along fractures associated with fault systems (Han et al., 2006). A geological environment such as this makes it easier for radon to migrate upwards because fracture zones serve as pathways for dissolved radon (Cho et al., 2015).

Fractures and faults evidently play an important role in the transportation of radon gas, and faults with different structural features provide different types of escape channels. Based on the degree of rock deformation, a fault zone can be divided into a fault core, a damage zone, and wall rock (Ben-Zion and Sammis, 2003), with each zone having distinct fluid-transport properties. The fault core likely exists as a slip plane containing a clay-rich fault gouge, or as a highly consolidated zone of shattered rocks. The fault core is as narrow as 2–3 mm in small faults, and is 10–20 cm wide in large faults. Despite its narrowness, most of the overall deformation is accommodated in the fault core. In comparison to the fault core, the damage zone is relatively large, usually being as large as several hundred meters wide, but weakly deformed. Typically, minor faults, fractures, and folds are fairly evenly developed throughout the damage zone. Within the wall rocks beyond the damage zone, there is almost no deformation.

Based on the role of the fault core in fluid transport, either as a conduit or barrier to flow, four types of fault zones have been identified (Caine et al., 1996): partial water-conducting fault zones, water-conducting fault zones, partial water-resisting fault zones, and composite water-conducting/water-resisting fault zones (Fig. 8). Together, these represent the different end-member fluid-transportation regimes that are encountered over the course of fault evolution. A newly formed fault likely has only one fracture plane with a small displacement. Therefore, the permeability of this fracture plane is relatively high, leading to the formation of a partially water-conducting fault zone. As this fault zone continues to grow, a grid-like damage zone may develop along both sides of the main fracture-plane, enhancing the permeability of the fault zone and thus forming a water-conducting fault zone. However, there is also the possibility that no damage zone is created, in which case fault gouge and shattered rocks in the core act as a barrier to fluid transportation, leading to the formation of a partially water-resisting fault zone. In comparison, water-conducting/water-resisting composite fault zones are most common in nature, as fault gouge and shattered rocks act as barriers to fluid transportation in their core, but relatively high permeabilities are seen in the damage zones on either side of the core.

The composition and structure of a fault core and damage

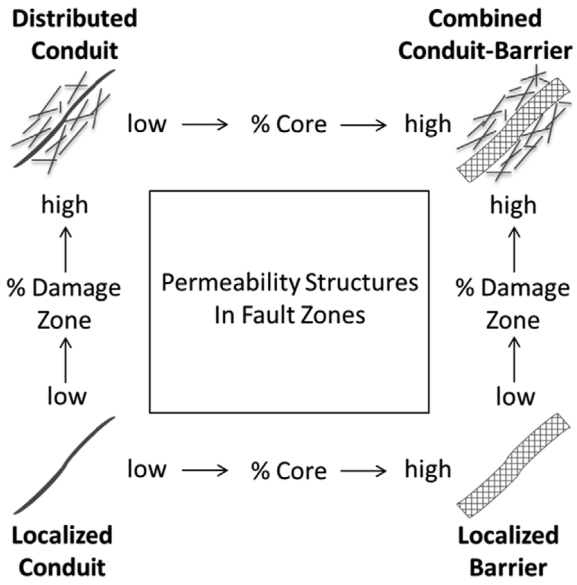

Fig. 8. Conceptual scheme of fault-related fluid flow (according to Caine et al., 1996).

http://dx.doi.org/10.1007/s12303-017-0028-2

zone directly affect the efficiency of radon gas escape to the ground surface and atmosphere (Fig. 8). A fault with a large number of fractures in its damage zone and a high-permeability fault core provides ideal conditions for radon gas escape. High radon concentrations are therefore found in soil gas at such faults. On the other hand, if no fractures have formed in the damage zone and the fault core is impermeable, radon gas cannot escape from the subsurface and radon concentrations in soil gas are low.

5.2. Effects of Strain across Faults on Radon Concentrations in Soil Gas

Seminsky and Bobrov (2009) reported the results of radon surveys across 26 faults of varying size and orientation in areas of the western Baikal and southern Angara, southern Siberian craton. Faults appeared in their radon concentration maps as broad zones of high radon activity that are 1.4 times the width of faulting-related deformation zones. When all other factors are equal, the radon emission rate depends on the size and slip geometry of faults, along with their Cenozoic activity rates. Radon release is relatively high in rift-related faults relative to cratonic faults, normal faults relative to strike-slip faults, and larger and more active faults, with activity being the basic geodynamic control on radon emanation.

The formation of new fractures not only favors the generation of more radon gas, but also provides channels for radon gas transport. However, if fractures that were originally open are closed, these channels will be blocked and radon transport impeded. Accordingly, in faults and associated damage zones experiencing different states of strain across faults, fractures may have different opening and closing states, affecting the permeability of the fault core and associated damage zone and giving rise to varying spatial distributions of soil-gas radon concentrations at the ground surface.

For normal faults (Fig. 9a), the strain across the fault may be extensional, resulting in relatively high permeabilities and thus favoring the diffusion of radon gas from the crust to the surface and atmosphere. As a result, soil-gas radon concentrations across normal faults are usually highest at the fault, and decrease gradually away from the fault on either side before converging to a constant value at distance. An example of this behavior is seen across the BLT fault zone at Korla (Fig. 7).

At thrust faults (Fig. 9b), the strain across the faults is

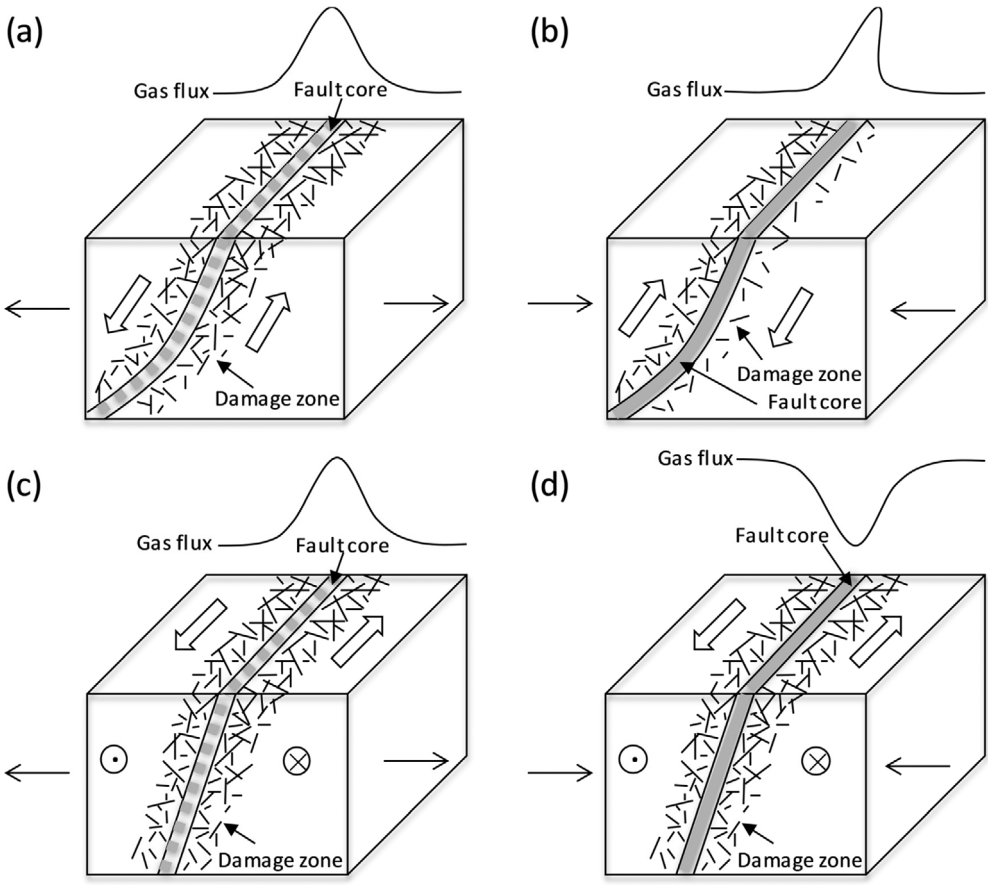

Fig. 9. Illustrations of the relationship between strain regime and radon concentration in soil gas at (a) a normal fault, (b) a thrust, (c) a transtensional fault, and (d) a transpressional fault.

contractional. The fault core is mostly made up of a low-permeability or water-resisting fault gouge, and fractures in the footwall are mostly closed. Both of these conditions hamper the upward migration of radon gas. In addition, thrusting causes the hanging wall to be highly deformed near to the fault at the surface, resulting in local bending and extensional fractures that facilitate the upward escape of radon gas. Therefore, soil-gas radon concentrations at thrust faults usually increase in the hanging wall approaching the fault, but drop abruptly at the fault, with the footwall typically having relatively low concentrations. An example of this behavior is seen across the BLT fault zone at Tiemenguan (Fig. 6).

As strike-slip fault with extension across the fault, the fault core and damage zone both contain abundant extensional fractures (Fig. 9c), similar to the case of a normal fault. Soil-gas radon concentrations recorded across such faults usually peak at the fault, and decrease gradually away from the fault on either side before converging to a constant value at distance. If the strain is contractional, then the fault core and damage zone may contain closed fractures (Fig. 9d). In this case, measured soil-gas radon concentrations are usually lowest at the fault and increase gradually away from the fault on either side before converging to a constant value at distance. An example of this behavior is seen in the profiles across the HY fault presented in this study (Fig. 5).

5.3. Relationship between Geological Factors and Radon Concentration

Geology is known to be the most important factor controlling the source and distribution of radon (Appleton and Miles, 2010). Relatively high levels of radon emissions are associated with particular types of bedrock and unconsolidated deposits such as some, but not all, granites, limestones, ironstones, phosphatic rocks, and shale-rich inorganic materials (Scheib et al., 2013). A relationship between geology and frequency ratio has been identified, implying a strong correlation between radon levels and bedrock type. Granite and granitic rocks, such as

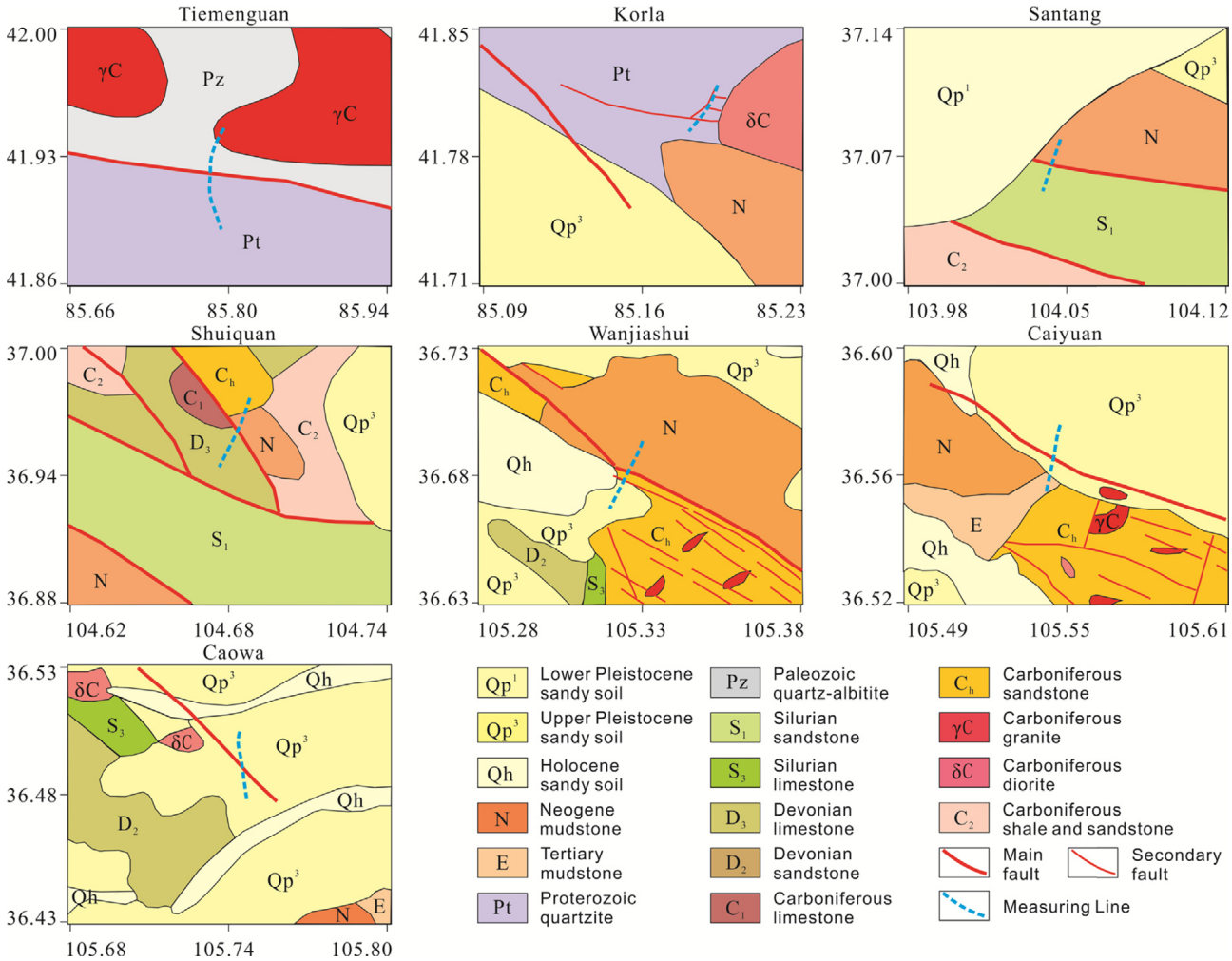

Fig. 10. Geological maps of the areas around the seven survey lines presented in this study.

http://dx.doi.org/10.1007/s12303-017-0028-2

granitic gneiss, have the highest frequency ratios for high radon levels, such as for basic Paleozoic volcanic rocks. Sedimentary rocks, volcanic rocks, anorthosite, and some metasedimentary rocks have low frequency ratios and low radon levels (e.g., the Ogcheon Group, Korea; Cho et al., 2015).

Figure 10 shows geological maps of the areas surrounding the seven survey lines used in this study. Except for at Korla and Caowa, different lithologies are seen on either side of the fault. By combining these maps with Figures 4b, 5, and 6b, we can see that although radon concentrations at the fault are low, there are clear differences on either side of the fault. For example, the profile at Santang shows that radon concentrations above Neogene mudstone are higher than above Silurian sandstone. A similar result is seen at Shuiquan, with Neogene mudstone having higher radon concentrations than Devonian sandstone; radon concentrations appear to rapidly decline in the lower Pleistocene sandy soil.

Although lithology is an important factor controlling the source and distribution of radon, as shown in this study, significant spatial variations in radon concentration are seen as a function of perpendicular distance from a fault. Thus, we hypothesize that the extent of fracture development is the most important control on radon concentration, as these fractures enables radon to migrate and escape into the atmosphere from the subsurface.

5.4. Effects of Other Factors on Radon Concentration in Soil Gas

The radon concentration in soil gas is influenced by factors other than fracture development and the regional tectonic stress field. Radon emissions are commonly measured in environments with high concentrations of CO_2; e.g., soil, caves, mofettes (natural CO_2 spring areas), and fumaroles adjacent to volcanoes (Heiligmann et al., 1997; Zimmer and Erzinger, 2003; Pérez et al., 2007; Papp et al., 2010; Phuong et al., 2012; Bonforte et al., 2013).

The short half-life of ^{222}Rn (3.82 days) means that it can only migrate a short distance through the ground by diffusion, limited to a few meters. To travel greater distances, radon needs a carrier fluid, either in gaseous or liquid form. Groundwater, or gases such as CO_2, CH_4, and N_2 that are found in a wide range of geological settings, can act as this carrier fluid. Laboratory experiments using various carrier gases suggest that CO_2 is the most effective fluid for radon transport (Chyi et al., 2010). The carrier-fluid velocity depends on the pressure gradient and fracture width, and rapid fluid ascent is possible in the presence of gas bubbles (Etiope and Martinelli, 2002). Given the importance of carrier fluid, it is somewhat surprising that systematic studies of radon and its carrier fluids in geological settings are rare (Heinicke et al., 1995; Perrier et al., 2009).

Therefore, the migration and transportation of trace gases such as radon to the ground surface are also controlled by the availability of geogenic CO_2, which acts as a carrier medium (Kemski et al., 1996; Ciotoli et al., 1999; Yang et al., 2005). On the other hand, dilution of radon by prevailing CO_2 in fractured zones can result in very low measured radon values; the highest radon levels coincide with locations with the lowest CO_2 flux (Zarroca et al., 2012).

6. CONCLUSION

Measurements of radon concentrations in soil gas were made across different types of fault zones, so that the spatial variation in radon concentrations could be characterized across different styles of fault located in different tectonic environments. The following results were obtained.

(1) The permeability of a fault zone plays a significant role in controlling the variation in soil-gas radon concentrations across a fault. If the fault zone contains many extensional fractures and therefore has high permeability, it is easy for radon gas at depth to move to the surface and atmosphere, resulting in relatively high soil gas concentrations. However, if the fault zone and its fractures are closed under with contraction aross them and thus have low permeability, it is difficult for deep radon gas to diffuse upward, meaning the soil gas has low radon concentrations.

(2) The strain across a normal fault is extensional, which may favor the diffusion of radon gas from the crust to the ground surface and atmosphere. Therefore, at normal faults, soil-gas radon concentrations are usually highest at the fault and decrease gradually with distance from the fault. A thrust fault and its surrounding region are associated with contractional strain. In this situation, the fault core and fractures in the footwall are mostly closed, acting as a barrier to the upward escape of radon gas, while extensional fractures in the hanging wall near the fault, resulting from local bending, assist the escape of radon. Therefore, soil-gas radon concentrations in the hanging wall of thrust zones gradually increase approaching the fault, and drop abruptly at the fault. For strike-slip fault with extension across the fault, soil-gas radon concentrations are relatively high at the fault, and decrease gradually with distance from the fault. For strike-slip fault with contraction across the fault, soil-gas radon concentrations are relatively low at the fault, and increase gradually with distance from the fault.

ACKNOWLEDGMENTS

The field work for this study was supported by the Seismological

Bureau of Gansu Province, the Seismological Bureau of Ningxia Hui Autonomous Region, and the Haiyuan seismological station. The authors thank Guomeng Zhang and Lei Zhang of the Institute of Crustal Dynamics of the China Seismological Bureau, Bo Wang of the China Earthquake Networks Center, Zhen Fang of the Seismological Bureau of Anhui Province, Hejun Su of the Seismological Bureau of Gansu Province, and Long Yan of the Seismological Bureau of Xinjiang Uyghur Autonomous Region for help with field measurements. This work was supported financially by the Research Grant from Institute of Crustal Dynamics, China Earthquake Administration (ZDJ2017-27), the National Natural Science Foundation of China (41502239), and the Seismological Industry Research Special Fund of China (201408019-03).

REFERENCES

Abdallah, S.M., Habib, R.R., Nuwayhid, R.Y., Chatila, M., and Katul, G., 2007, Radon measurements in well and spring water in Lebanon. Radiation Measurements, 42, 298–303.

Appleton, J.D. and Miles, J.C.H., 2010, A statistical evaluation of the geogenic controls on indoor radon concentrations and radon risk. Journal of Environmental Radioactivity, 101, 799–803.

Baykara, O., İnceöz, M., Doğru, M., Aksoy, E., and Külahcı, F., 2009, Soil radon monitoring and anomalies in East Anatolian Fault System (Turkey). Journal of Radioanalytical and Nuclear Chemistry, 279, 159–164.

Ben-Zion, Y. and Sammis, C.G., 2003, Characterization of fault zones. Pure and Applied Geophysics, 160, 677–715.

Bonforte, A., Federico, C., Giammanco, S., Guglielmino, F., Liuzzo, M., and Neri, M., 2013, Soil gases and SAR measurements reveal hidden faults on the sliding flank of Mt. Etna (Italy). Journal of Volcanology and Geothermal Research, 251, 27–40.

Caine, J.S., Evans, J.P., and Forster, C.B., 1996, Fault zone architecture and permeability structure. Geology, 24, 1025–1028.

Catalano, R., Immè, G., Mangano, G., Morelli, D., Aranzulla, M., Giammanco, S., and Thinova, L., 2015, In situ and laboratory measurements for radon transport process study. Journal of Radioanalytical and Nuclear Chemistry, 306, 673–684.

Cavalié, O., Lasserre, C., Doin, M.-P., Peltzer, G., Sun, J., Xu, X., and Shen, Z.-K., 2008, Measurement of interseismic strain across the Haiyuan fault (Gansu, China), by InSAR. Earth and Planetary Science Letters, 275, 246–257.

Cho, B.-W., Choo, C.O., Kim, M.S., Hwang, J., Yun, U., and Lee, S., 2015, Spatial relationships between radon and topographical, geological, and geochemical factors and their relevance in all of South Korea. Environmental Earth Sciences, 74, 5155–5168.

Choubey, V.M., Bartarya, S.K., Saini, N.K., and Ramola, R.C., 2001, Impact of geohydrology and neotectonic activity on radon concentration in groundwater of intermontane Doon Valley, Outer Himalaya, India. Environmental Geology, 40, 257–266.

Choubey, V.M., Bist, K.S., Saini, N.K., and Ramola, R.C., 1999, Relation between soil-gas radon variation and different lithotectonic units, Garhwal Himalaya, India. Applied Radiation and Isotopes, 51, 587–592.

Chyi, L.L., Quick, T.J., Yang, T.F., and Chen, C.H., 2010, The experimental investigation of soil gas radon migration mechanisms and its implication in earthquake forecast. Geofluids, 10, 556–563.

Ciotoli, G., Etiope, G., Guerra, M., and Lombardi, S., 1999, The detection of concealed faults in the Ofanto Basin using the correlation between soil-gas fracture surveys. Tectonophysics, 301, 321–332.

Cosma, C., Cucoş (Dinu), A., Papp, B., Begy, R., Gabor, A., Bican-Brişan, N., and Beşuţiu, L., 2014, Radon implication in life and earth science: Băiţa-Ştei area and Peceneaga-Camena fault (Romania). Carpathian Journal of Earth and Environmental Sciences, 9, 15–21.

Etiope, G. and Martinelli, G., 2002, Migration of carrier and trace gases in the geosphere: an overview. Physics of the Earth and Planetary Interiors, 129, 185–204.

Giammanco, S., Immè, G., Mangano, G., Morelli, D., and Neri, M., 2009, Comparison between different methodologies for detecting radon in soil along an active fault: the case of the Pernicana fault system, Mt. Etna (Italy). Applied Radiation and Isotopes, 67, 178–185.

Han, Y.L., Kuo, M.C.T., Fan, K.C., Chiang, C.J., and Lee, Y.P., 2006, Radon distribution in groundwater of Taiwan. Hydrogeology Journal, 14, 173–179.

Heiligmann, M., Stix, J., Williams-Jones, G., Lollar, B.S., and Garzón, V.G., 1997, Distal degassing of radon and carbon dioxide on Galeras volcano, Colombia. Journal of Volcanology and Geothermal Research, 77, 267–283.

Heinicke, J., Koch, U., and Martinelli, G., 1995, CO_2 and radon measurements in the Vogtland Area (Germany) – a contribution to earthquake prediction research. Geophysical Research Letters, 22, 771–774.

Idriss, H., Salih, I., Alaamer, A.S., Abdelgalil, M.Y., Salih, S.A., Hasan, A.M., Eltahir, M.A., and Ahamed, M.M.O., 2014, Study of radon in soil gas, trace elements and climatic parameters around South Kordofan state, Sudan. Environmental Earth Sciences, 72, 335–339.

Immè, G., La Delfa, S., Lo Nigro, S., Morelli, D., and Patanè, G., 2006, Soil radon concentration and volcanic activity of Mt. Etna before and after the 2002 eruption. Radiation Measurements, 41, 241–245.

Jönsson, G., Baixeras, C., Devantier, R., Enge, W., Font, L.I., Freyer, K., and Treutler, H.-C., 1999, Soil radon levels measured with SSNTD's and the soil radium content. Radiation Measurements, 31, 291–294.

Kemski, J., Klingel, R., and Siehl, A., 1996, Classification and mapping of radon-affected areas in Germany. Environment International, 22, 789–798.

King, C.-Y., Koizumi, N., and Kitagawa, Y., 1995, Hydrogeochemical anomalies and the 1995 Kobe earthquake. Science, 269, 38–39.

King, C.-Y., King, B.-S., Evans, W.C., and Zhang, W., 1996, Spatial radon anomalies on active faults in California. Applied Geochemistry, 11, 497–510.

Kobeissi, M.A., El-Samad, O., and Rachidi, I., 2013, Health assessment of natural radioactivity and radon exhalation rate in granites used as building materials in Lebanon. Radiation Protection Dosimetry, 153, 342–351.

Kobeissi, M.A., El Samad, O., Zahraman, K., Milky, S., Bahsoun, F., and Abumurad, K.M., 2008, Natural radioactivity measurements in building materials in southern Lebanon. Journal of Environmental

 http://dx.doi.org/10.1007/s12303-017-0028-2

Radioactivity, 99, 1279–1288.

Kobeissi, M.A., Gomez, F., and Tabet, C., 2015, Measurement of anomalous radon gas emanation across the Yammouneh Fault in southern Lebanon: a possible approach to earthquake prediction. International Journal of Disaster Risk Science, 6, 250–266.

La Delfa, S., Immè, G., Lo Nigro, S., Morelli, D., Patanè, G., and Vizzini, F., 2007, Radon measurements in the SE and NE flank of Mt. Etna (Italy). Radiation Measurements, 42, 1404–1408.

Linde, A.T. and Sacks, I.S., 1998, Triggering of volcanic eruptions. Nature, 395, 888–890.

Liu-Zeng, J., Klinger, Y., Xu, X., Lasserre, C., Chen, G., Chen, W., Tapponnier, P., and Zhang, B., 2007, Millennial recurrence of large earthquakes on the Haiyuan Fault near Songshan, Gansu Province, China. Bulletin of the Seismological Society of America, 97, 14–34.

Luo, F.Z. and Xiang, Z.Y., 2002, New activity traces of active faults nearby Kuerle, Xinjiang. Inland Earthquake, 16, 148–153. (In Chinese)

Mazur, D., Janik, M., Łoskiewicz, J., Olko, P., and Swakoń, J., 1999, Measurements of radon concentration in soil gas by CR-39 detectors. Radiation Measurements, 31, 295–300.

Mollo, S., Tuccimei, P., Heap, M.J., Vinciguerra, S., Soligo, M., Castelluccio, M., Scarlato, P., and Dingwell, D.B., 2011, Increase in radon emission due to rock failure: an experimental study. Geophysical Research Letters, 38, L14304.

Mudd, G.M., 2008, Radon releases from Australian uranium mining and milling projects: assessing the UNSCEAR approach. Journal of Environmental Radioactivity, 99, 288–315.

Namvaran, M. and Negarestani, A., 2013, Measuring the radon concentration and investigating the mechanism of decline prior an earthquake (Jooshan, SE of Iran). Journal of Radioanalytical and Nuclear Chemistry, 298, 1–8.

Nazaroff, W.W., 1992, Radon transport from soil to air. Reviews of Geophysics, 30, 137–160.

Neri, M., Behncke, B., Burton, M., Galli, G., Giammanco, S., Pecora, E., Privitera, E., and Reitano, D., 2006, Continuous soil radon monitoring during the July 2006 Etna eruption. Geophysical Research Letters, 33, L24316.

Neri, M., Giammanco, S., Ferrera, E., Patanè, G., and Zanon, V., 2011, Spatial distribution of soil radon as a tool to recognize active faulting on an active volcano: the example of Mt. Etna (Italy). Journal of Environmental Radioactivity, 102, 863–870.

Neri, M., Guglielmino, F., and Rust, D., 2007, Flank instability on Mount Etna: Radon, radar interferometry, and geodetic data from the southwestern boundary of the unstable sector. Journal of Geophysical Research: Solid Earth, 112, B04410.

Papp, B., Szakács, A., Néda, T., Papp, Sz., and Cosma, C., 2010, Soil radon and thoron studies near the mofettes at Harghita Bai (Romania) and their relation to the field location of fault zones. Geofluids, 10, 586–593.

Pérez, N.M., Hernández, P.A., Padrón, E., Melián, G., Marrero, R., Padilla, G., Barrancos, J., and Nolasco, D., 2007, Precursory subsurface ^{222}Rn and ^{220}Rn degassing signatures of the 2004 seismic crisis at Tenerife, Canary Islands. Pure and Applied Geophysics, 164, 2431–2448.

Perrier, F., Richon, P., Byrdina, S., France-Lanord, C., Rajaure, S., Koirala, B.P., Shrestha, P.L., Gautam, U.P., Tiwari, D.R., Revil, A., Bollinger, L., Contraires, S., Bureau, S., and Sapkota, S.N., 2009, A direct evidence for high carbon dioxide and radon-222 discharge in Central Nepal. Earth and Planetary Science Letters, 278, 198–207.

Phuong, N.K., Harijoko, A., Itoi, R., and Unoki, Y., 2012, Water geochemistry and soil gas survey at Ungaran geothermal field, central Java, Indonesia. Journal of Volcanology and Geothermal Research, 229–230, 23–33.

Przylibski, T.A., 2000, Estimating the radon emanation coefficient from crystalline rocks into groundwater. Applied Radiation and Isotopes, 53, 473–479.

Roeloffs, E., 1999, Earth science: radon and rock deformation. Nature, 399, 104–105.

Scheib, C., Appleton, J.D., Miles, J.C.H., Hodgkinson, E., 2013, Geological controls on radon potential in England. Proceedings of the Geologists' Association, 124, 910–928.

Seminsky, K.Zh. and Bobrov, A.A., 2009, Radon activity of faults (western Baikal and southern Angara areas). Russian Geology and Geophysics, 50, 682–692.

Siniscalchi, A., Tripaldi, S., Neri, M., Giammanco, S., Piscitelli, S., Balasco, M., Behncke, B., Magri, C., Naudet, V., and Rizzo, E., 2010, Insights into fluid circulation across the Pernicana Fault (Mt. Etna, Italy) and implications for flank instability. Journal of Volcanology and Geothermal Research, 193, 137–142.

Somlai, K., Tokonami, S., Ishikawa, T., Vancsura, P., Gáspár, M., Jobbágy, V., Somlai, J., and Kovács, T., 2007, ^{222}Rn concentrations of water in the Balaton Highland and in the southern part of Hungary, and the assessment of the resulting dose. Radiation Measurements, 42, 491–495.

Sulochana, V., Francis, A., and Tickle, A., 2015, Morphology based radon processed neural network for transmission line fault detection. Proceedings of the 4th International Conference on Advances in Computing, Communications and Informatics, Kerala, Aug. 10–13, p. 1137–1143.

Tabar, E. and Yakut, H., 2014, Radon measurements in water samples from the thermal springs of Yalova basin, Turkey. Journal of Radioanalytical and Nuclear Chemistry, 299, 311–319.

Trique, M., Richon, P., Perrier, F., Avouac, J.P., and Sabroux, J.C., 1999, Radon emanation and electric potential variations associated with transient deformation near reservoir lakes. Nature, 399, 137–141.

Tuccimei, P., Mollo, S., Soligo, M., Scarlato, P., and Castelluccio, M., 2015, Real-time setup to record radon emission during rock deformation: implications for geochemical surveillance. Geoscientific Instrumentation, Methods and Data Systems Discussions, 5, 39–62.

Tuccimei, P., Mollo, S., Vinciguerra, S., Castelluccio, M., and Soligo, M., 2010, Radon and thoron emission from lithophysae-rich tuff under increasing deformation: an experimental study. Geophysical Research Letters, 37, L05305.

Wattananikorn, K., Techakosit, S., and Jitaree, N., 1995, A combination of soil gas radon measurements in uranium exploration. Nuclear Geophysics, 9, 643–652.

Wiegand, J., 2001, A guideline for the evaluation of the soil radon potential based on geogenic and anthropogenic parameters. Environmental Geology, 40, 949–963.

Yang, T.F., Walia, V., Chyi, L.L., Fu, C.C., Chen, C.-H., Liu, T.K., Song,

S.R., Lee, C.Y., and Lee, M., 2005, Variations of soil radon and thoron concentrations in a fault zone and prospective earthquakes in SW Taiwan. Radiation Measurements, 40, 496–502.

Zahorowski, W., Chambers, S.D., and Henderson-Sellers, A., 2004, Ground based radon-222 observations and their application to atmospheric studies. Journal of Environmental Radioactivity, 76, 3–33.

Zarroca, M., Linares, R., Bach, J., Roqué, C., Moreno, V., Font, Ll., and Baixeras, C., 2012, Integrated geophysics and soil gas profiles as a tool to characterize active faults: the Amer fault example (Pyrenees, NE Spain). Environmental Earth Sciences, 67, 889–910.

Zimmer, M. and Erzinger, J., 2003, Continuous H_2O, CO_2, ^{222}Rn and temperature measurements on Merapi volcano, Indonesia. Journal of Volcanology and Geothermal Research, 125, 25–38.

Žunić, Z.S., Kobal, I., Vaupotič, J., Kozak, K., Mazur, J., Birovljev, A., Janik, M., Čeliković, I., Ujić, P., Demajo, A., Krstić, G., Jakupi, B., Quarto, M., and Bochicchio, F., 2006, High natural radiation exposure in radon spa areas: a detailed field investigation in Niška Banja (Balkan region). Journal of Environmental Radioactivity, 89, 249–260.

http://dx.doi.org/10.1007/s12303-017-0028-2